Monthly Notices of the ROYAL ASTRONOMICAL SOCIETY

MNRAS **527,** 8131–8139 (2024) https://doi.org/10.1093/mnras/stad3621
Advance Access publication 2023 November 24

Radial compositional profile of Saturn's E ring indicates substantial space weathering effects

Lenz Nölle,[1]★ Frank Postberg,[1] Jürgen Schmidt,[1,2] Fabian Klenner,[3] Nozair Khawaja,[1] Jon Hillier,[1] Sascha Kempf,[4] Sean Hsu[4] and Ralf Srama[5]

[1]*Institute of Geological Sciences, Freie Universität Berlin, Malteserstraße 74-100, D-12249 Berlin, Germany*
[2]*Space Physics and Astronomy Research Unit, University of Oulu, P.O.Box 8000, FI-90014 Oulu, Finland*
[3]*Department of Earth and Space Sciences, University of Washington, 4000 15th Avenue NE, WA 98195 Seattle, USA*
[4]*Laboratory for Atmospheric and Space Physics, University of Colorado, 1234 Innovation Dr, CO 80303 Boulder, USA*
[5]*Institute of Space Systems, University of Stuttgart, Pfaffenwaldring 29, D-70569 Stuttgart, Germany*

Accepted 2023 November 20. Received 2023 July 26; in original form 2023 November 20

ABSTRACT

Saturn's large and diffuse E ring is populated by microscopic water ice dust particles, which originate from the Enceladus plume. *Cassini*'s Cosmic Dust Analyser sampled these ice grains, revealing three compositional particle types with different concentrations of salts and organics. Here, we present the analysis of CDA mass spectra from several orbital periods of *Cassini*, covering the region from interior to Enceladus' orbit to outside the orbit of Rhea, to map the distribution of the different particle types throughout the radial extent of the E ring. This will provide a better understanding of the potential impact of space weathering effects on to these particles, as the ice grains experience an increasing exposure age during their radially outward migration. In this context, we report the discovery of a new ice particle type (Type 5), which produces spectra indicative of very high salt concentrations, and which we suggest to evolve from less-salty Enceladean ice grains by space weathering. The radial compositional profile, now encompassing four particle types, reveals distinct radial variations in the E ring. At the orbital distance of Enceladus our results are in good agreement with earlier compositional analyses of E ring ice grains in the moon's vicinity. With increasing radial distance to Saturn however, our analysis suggests a growing degree of space weathering and considerable changes to the spatial distribution of the particle types. We also find that the proportion of Type 5 grains – peaking near Rhea's orbit – probably reflects particle charging processes in the E ring.

Key words: astrochemistry – methods: data analysis – planets and satellites: individual: Enceladus – planets and satellites: rings.

1. INTRODUCTION

Saturn's diffuse E ring is one of the largest known planetary rings in the Solar system. It spans radially from at least 2.5 R_{Saturn} (Linti et al., in preparation; Saturn equatorial radius $R_{Saturn} = 60\,268$ km), encompassing the orbits of the icy moons Mimas, Enceladus, Tethys, Dione, and Rhea, and extending at least to Titan's orbit at about 20 R_S (Kempf et al. 2008; Srama et al. 2011). Besides that, it extends thousands of kilometers vertically away from the equatorial (ring) plane (Nicholson et al. 1996; de Pater, Martin & Showalter 2004; Porco et al. 2006; Kempf et al. 2008). Enceladus was an early candidate as the main source of the E ring, as the ring's edge-on brightness profile peaks near the moon's mean orbital distance (Baum et al. 1981; Showalter, Cuzzi & Larson 1991). Now known to be primarily composed of μm to sub-μm sized water ice dust (Hillier et al. 2007a; Postberg et al. 2008), nearly 40 years ago the photometric properties of the ring were found to be a good match to spherical ice particles with a narrow size distribution, for which (cryo)volcanic liquid water emission was suggested as a source (Pang et al. 1984; Showalter et al. 1991). Later observations with the instruments onboard the *Cassini* orbiter ultimately confirmed this, when cryo-volcanoes along the so-called tiger stripes fractures, cross cutting the icy crust at the south polar terrain of Enceladus, were discovered (Dougherty et al. 2006; Porco et al. 2006; Spahn et al. 2006a). A plume of gas and water vapour (Dougherty et al. 2006; Hansen et al. 2006; Waite et al. 2006) is ejected from the tiger stripes into space, carrying the microscopic water ice particles (Porco et al. 2006; Spahn et al. 2006a, b; Hillier et al. 2007a; Schmidt et al. 2008). Most of the emitted grains fall back on to the surface of Enceladus (Kempf, Beckmann & Schmidt 2010) while a substantial part (≈10 per cent) escapes the moon's Hill sphere, forming and sustaining the E ring (Spahn et al. 2006a, b; Kempf et al., 2010, 2018). The discovery of salts in about 10 per cent of these E ring ice particles (Postberg et al. 2009a) and in an even larger proportion of plume grains (Postberg et al. 2011) indicates the existence of a subsurface ocean, the source of the water ice grains and vapour, beneath Enceladus' ice crust.

The *Cassini* spacecraft, launched in 1997, was a flagship mission by NASA, European Space Agency (ESA), and the Italian Space

★ E-mail:lenz.noelle@fu-berlin.de

Agency (ASI), with the goal of investigating the Saturn system. After its arrival on 2004 July 1, it operated until 2017 September 15, when it plunged into Saturn's atmosphere. One of its instruments was the Cosmic Dust Analyser (CDA), an impact-ionization dust detector, designed to examine the properties of planetary, interplanetary, and interstellar dust particles in the Saturnian system (Srama et al. 2004). For this purpose, it had multiple subsystems to determine dust particle masses, surface charges, impact velocities, fluxes, and compositions. The latter was determined by CDA's chemical analyser (CA) subunit, a linear impact ionization time of flight mass spectrometer, which produced basic chemical analyses of the material from impacting dust particles (Srama et al. 2004; Postberg et al. 2009b).

During *Cassini*'s numerous orbits passing through the E ring, the CDA recorded hundreds of thousands of mass spectra of the ring's icy dust particles. Previous analyses of these mass spectra revealed three main compositional classes of icy dust particles in the E ring, which all are proposed to originate – directly or indirectly – oceanic water inside the tiger stripe fractures. The first and most abundant particle type (i. e. Type 1) is one of almost pure water ice with only minor traces of salts (Postberg et al., 2008, 2009a). This type of particle is presumably formed by the condensation and freezing of water vapour in the ice vents, within the crust of Enceladus beneath the tiger stripes (Postberg et al. 2018b; Cable et al. 2021). The second particle type (Type 2) describes ice particles with a detectable content of organic substances (Postberg et al. 2018a; Khawaja et al. 2019). For this population, two different formation mechanisms are currently considered to be at work in parallel: adsorption of volatile, low-mass organics on to Type 1 ice particles and refractory organic spray droplets, rich in high-mass organics produced by bubble bursting at the ocean water surface, that are subsequently enveloped by ice from condensing water vapour in the ice vents (Postberg et al. 2018b; Cable et al. 2021). The third type (Type 3) are water ice particles strongly enriched in salts (Postberg et al. 2009a). These likely form by freezing of oceanic water droplets, produced by turbulence of the water surface (Postberg et al. 2009a; Cable et al. 2021). These properties are summarized in Table S1.

So far, the proportions of these three compositional types have only been investigated for Enceladus' plume (Postberg et al. 2011) and the inner E ring (Postberg et al. 2009a). In this work, we present the first, comprehensive, radial compositional map through the E ring, based on *Cassini* CDA data from several low inclination, equatorial E ring plane passages. We also aim to find compositional evidence of alteration of these icy dust particles with radial position, by e.g. space weathering effects. During the dust particles' lifetimes of up to more than one century (Horányi, Juhász & Morfill 2008) they slowly migrate outwards, increasing their semimajor axes, due to co-rotational drag from the Saturnian plasma (e.g. Dekarev et al. 1998). This statistically links the particles' ages to their average distance to Saturn upon detection, making a radial, compositional map a promising target to look for the impact of space weathering. Furthermore, we discuss a newly discovered E ring particle type with respect to its mass spectral and dynamic properties, to infer its spatial origin and formation mechanism as well as its possible link to space weathering processes. In this context, we present the results of a dedicated laboratory analogue measurement campaign with the laser-induced liquid beam ion desorption (LILBID) time-of-flight mass spectrometer at Freie Universität Berlin. By comparing these LILBID analogue spectra with the respective CDA spectra, as similarly done before for the main particle types (e.g. Postberg et al. 2009a), we are able to put first constraints on the exact particle composition of this new type.

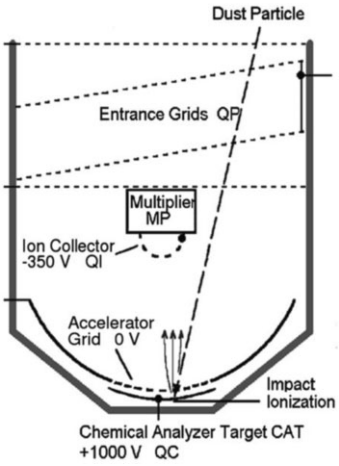

Figure 1. Schematic cross section of the CDA dust analyser subunit (Postberg et al. 2006). Depicted are its different parts and the attached charge amplifier channels.

2. INSTRUMENTS AND DATA ANALYSIS

2.1. Analysis of CDA mass spectra

The CDA instrument and its various parts have been described in detail by Srama et al. (2004). Here, we focus on CDA's dust analyser (DA) unit (Fig. 1) and in particular the CA subsystem, a simple, impact-ionization, linear time-of-flight mass spectrometer. Positive ions, generated during hypervelocity dust particle impacts on the rhodium CA target (CAT; see Fig. 1), are accelerated towards the multiplier (MP) by the strong electrostatic field between the CAT and the accelerator grid. The majority of the subsequent path to the MP is in a low-field drift region, causing the ions' separation based on their mass-to-charge ratios (m/z). Ion arrival times (t_i) are related to their masses (m_i) via the relation $t_i = a\sqrt{m_i} + t_0$, where a, the 'stretch' parameter is related to the instrument field configuration and geometry and t_0, the 'shift' parameter, is related to instrument triggering, as will be discussed below.

For the spectra considered in this work, recording of a mass spectrum was triggered only when the signal of one of two charge amplifier channels (Fig. 1; QC at the CAT or QM at the MP) exceeded a preassigned threshold. Thus, we distinguish different cases: (a) impact trigger – the impact signal, measured by the QC channel, exceeded the assigned QC trigger threshold; (b) line trigger – here the first ion species, arriving at MP, created a signal strong enough to exceed the trigger threshold of the QM channel. This happened either when the impact signal was too weak to exceed the QC trigger threshold or by design, when the QC channel was not enabled as a trigger. In case (b) spectrum recording started after a delay corresponding to the time-of-flight (ToF) of the triggering ion species. This time delay is represented by t_0 (shift parameter) and its value, which varies from spectrum to spectrum, reflects the respective trigger types. t_0 values of 0 to -0.4 µs are characteristic for an impact trigger, whereas t_0 values of around -0.5 µs and smaller are typical for line triggering, in most cases corresponding to the ToF of the triggering ion species. Typical triggering ion species are $^1H^+$ ($m/z \approx 1$ u; $t_0 \approx -0.48 \pm 0.05$ µs), $[^1H_3{}^{16}O]^+$ ($m/z \approx 19$ u; $t_0 \approx -2.05 \pm 0.1$ µs) or $^{23}Na^+$ ($m/z \approx 23$ u; $t_0 \approx -2.25 \pm 0.1$ µs). Due to an instrument incident in autumn 2008, possibly linked to the fast, deep dive through the Enceladus plume during the E5 flyby (see Postberg et al. 2011), the QC channel

experienced a massive sensitivity loss, effectively rendering impact-triggered spectra impossible. Since then, the line triggering is the only relevant CDA CA trigger mechanism for E ring ice grains. The stretch parameter a is defined by the instrument's geometry and field strengths. Previous works with CDA spectra suggest values between approximately 470 and 480 ns, with about 477 ns being the theoretical value for the nominal instrument voltages and zero initial energy ions. Here, a cross-correlation approach was used to determine the exact values of t_0 and a, adapted from Postberg et al. (2006, 2008, 2018a). We refer to these publications for further details about the mass spectrum generation and calibration process. Following the individual calibration, the mass spectra are classified based on the presence and/or absence of mass lines of characteristic ion species, based on the results from previous analyses of CDA mass spectra (Table S1).

For the radial compositional mapping of the E ring, only CDA spectra were considered, that were recorded during periods when *Cassini* passed though the E ring close to Saturn's equatorial ring plane (RPL, $|d_{RPL}| < 0.1$ R_{Saturn}; Table S2). This geometrical constraint was chosen to avoid introducing bias to the inferred radial compositional profile by possible vertical, compositional variations of the ring. A potential remaining bias is the periodic change in CDA's boresight (CDA–BS). Depending on whether CDA was the prioritized instrument or whether other instruments were given priority for their observations, CDA pointed into different directions during *Cassini*'s orbits. This resulted in frequent situations in which the angular distance between the CDA–BS and the reference influx direction for dust particles on circular orbits, called Dust–RAM, was larger than the aperture angle of the CAT subsystem of ± 28° (relative to CDA–BS; Srama et al. 2004). In such cases, the CAT was insensitive to the E ring particles with low to moderate orbital eccentricities, relevant for our analysis. Thus, all sections of the selected orbital periods during which the angle between the CDA–BS and Dust–RAM was > 25° are not considered for the spatial analysis, to reduce any bias introduced by dynamically different particles on highly eccentric orbits. Thus, from the 7536 actual spectra, found in the analysed periods (Table S2), 6370 are considered for the radial E ring mapping in this work. To produce the radial profile for the mapping, the spectra were sorted with respect to *Cassini*'s distance to Saturn at the moment of their detection. Starting at the lower distance limit, they are grouped into overlapping bins (50 per cent overlap) with a constant number of spectra per bin for comparable statistical error margins. Then, the spectral proportions and corresponding statistical errors are calculated for each spectral type and bin. A bin size of 720 spectra/bin has been selected for the radial mapping to achieve a good compromise between number of bins (spatial resolution) and sample size per bin (statistical error).

2.2. Laboratory analogue measurements

To investigate the composition of the new particle type (see Section 3.1), analogue measurements with the LILBID time-of-flight mass spectrometer at Freie Universität Berlin (Germany) of multiple, highly concentrated NaCl–KCl–H_2O mixtures were conducted. For a detailed description of the instrumental set-up, the working principle as well as the comparability with CDA's CA subsystem we refer to Klenner et al. (2019). All NaCl–KCl solutions were prepared with doubly distilled and deionized H_2O (18.2 MW 'Milli-Q') and the molar ratio of NaCl/KCl was adjusted to mimic $^{23}Na^+/^{39}K^+$ peak amplitude ratios of around 2–3. Overall salt concentrations ($= c_{NaCl} + c_{KCl}$) of 1, 2, and 4 mol L^{-1} were used to study the effect of growing salt concentrations. The spectrometer uses delayed ion extraction to simulate different CDA particle impact speed conditions, with a lower delay time corresponding to a higher impact speed and higher delay times corresponding to lower impact speeds (Klenner et al. 2019). Thus, to take into account the impact speed variations of our data (Table S2), ion extraction delay times of 4.9 and 5.1 μs were chosen. Because a single spectrum record from one laser shot on to the water beam exhibits a relatively high level of background noise, the instrument software co-adds a preset number of such single spectra to produce the final spectrum with a distinctly higher spectral *S/N*. For a good compromise between the degree of *S/N* enhancement and the accompanying increase of the measurement time/required sample volume, the number of single spectra to co-add was set to 300 spectra per measurement.

3. RESULTS

3.1. A new compositional type

The compositional analysis of CDA mass spectra from the selected periods (Table S2), revealed a new compositional type of E ring particles. In contrast to the three main types (Table S2; Fig. S1a–c), the characteristic spectral features of this type consist of only two peaks ($S/N \gg 3\sigma_{noise}$, $\sigma_{noise} \rightarrow$ uncertainty based on the individual spectral background noise), we call *main peaks*, corresponding to the mass lines $^{23}Na^+$ and $^{39}K^+$, and which indicate a salt-related composition. Other prominent mass lines, indicative e.g. for water are missing. Thus, extending the existing classification of three E ring ice particle types (Table S1) as well as a fourth type of non-E ring mineral dust (Altobelli et al. 2016; Fischer et al. 2018), we name this type 'Type 5'. In total, 180 spectra of this type have been identified (without BS filtering), which can be separated into two subpopulations based on the trigger case. Those with both main peaks (Fig. 2a) present (31 spectra) are subsequently referred to as 'early triggered' ($t_0 > -2$ µs). The remaining 149 were line triggered on $^{23}Na^+$, only show the $^{39}K^+$ mass line (Fig. 2b) and are called 'late triggered' ($t_0 < -2.15$ µs).

Tiny spectral signatures ($S/N < 3\sigma_{noise}$, Fig. S2), subsequently referred to as *minor peaks*, can be observed occasionally. Most minor peaks correspond to salt–cluster mass lines typically observed in CDA spectra of salt-bearing ice particles (Type 3; see Tables S1 and S3), further constraining the possible particle composition to a combination of salts and water ice. Impact speed dependent changes of the spectral appearance have not been observed as well as mass lines from the CA target material rhodium ($^{103}Rh^+$, $m/z = 103$ u) or CA target contaminants like carbon ($^{12}C^+$, $m/z = 12$ u). These mass lines typically occur in CDA mass spectra recorded at impact speeds exceeding 9 km s^{-1} (Postberg et al. 2009b) and thus their absence restricts the impact speed to this upper limit. Since this speed limit is in good agreement with the predicted Kepler–RAM speeds (Tables S2 and S4), Type 5 particles must exhibit comparable particle dynamics to the other E ring ice particles and thus their origin must be located inside the E ring.

As a next step, the $^{23}Na^+/^{39}K^+$ peak amplitude ratios were determined from early triggered spectra of sufficient spectral quality (Fig. 3). From the 31 early triggered spectra 15 – defined here as the Type 5 *archetypes* – are qualitatively good enough to be considered for this approach (see Table S4). Except for two outliers, the archetype spectra exhibit $^{23}Na^+/^{39}K^+$ peak ratios <3, with the overall average $^{23}Na^+/^{39}K^+$ peak ratio being located at 2.4. This level is more than one order of magnitude lower than in Type 3, that typically exhibit $^{23}Na^+/^{39}K^+$ peak amplitude ratios of >100 (Postberg et al. 2009a).

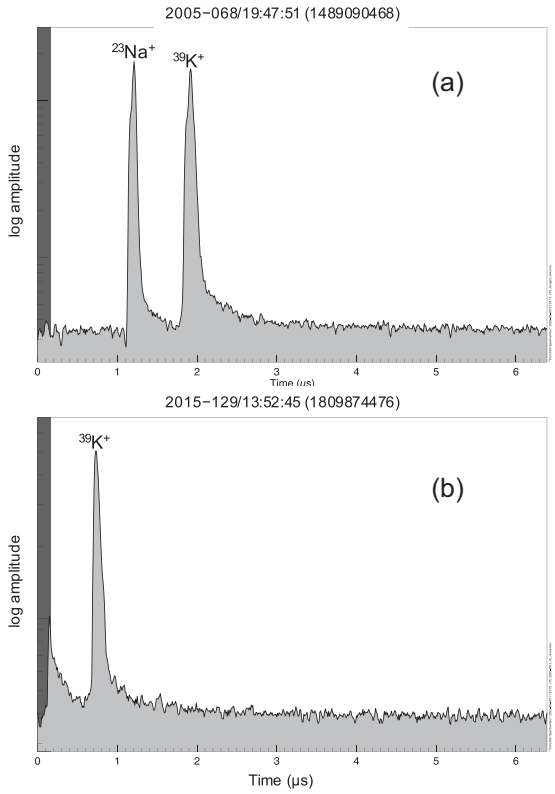

Figure 2. Type 5 example spectra: (a) Early triggered ($t_0 > -2$ μs); (b) Late triggered ($t_0 < -2.15$ μs).

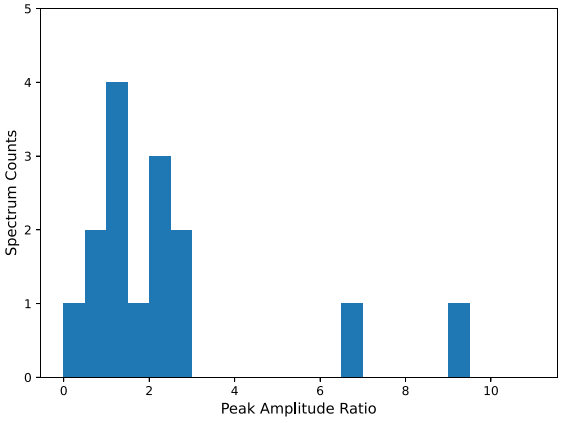

Figure 3. Distribution of the $^{23}Na^+/^{39}K^+$ peak amplitude ratios for the 15 archetype spectra of Type 5. Bin size = 0.5.

LILBID analogue experiments (Klenner et al. 2019) with highly concentrated salt-water solutions were conducted to constrain further the actual composition of the grains which produce Type 5 spectra. The $^{23}Na^+/^{39}K^+$ peak amplitude ratios observed in Type 5 spectra are reproduced best by a molar NaCl/KCl ratio of around 3–10 (see Fig. S3). The $^{23}Na^+/[^{23}Na^{35}Cl]^{23}Na^+$ peak amplitude ratio shows a clear increase with increasing overall salt concentration (Fig. 4). Based on this trend, the almost complete absence of the $[^{23}Na^{35}Cl]^{23}Na^+$ mass line in Type 5 spectra, except the rare occurrence as a minor mass line, suggests an overall salt concentration in the ice particles of >4 mol L^{-1}.

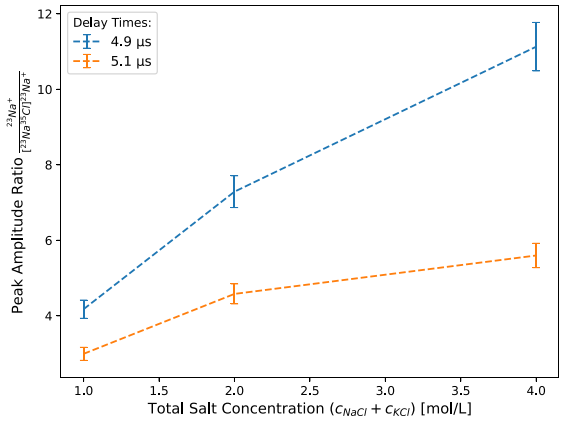

Figure 4. Peak amplitude ratios of $^{23}Na^+/[^{23}Na^{35}Cl]^{23}Na^+$ derived from LILBID measurements of NaCl–KCl–H_2O mixtures with a molar NaCl/KCl ratio of nine for different overall salt concentrations, measured at delay times of 4.9 and 5.1 μs. The depicted error bars represent the statistical error, since each measurement point has been derived from a spectrum itself being composed of 300 averaged spectra.

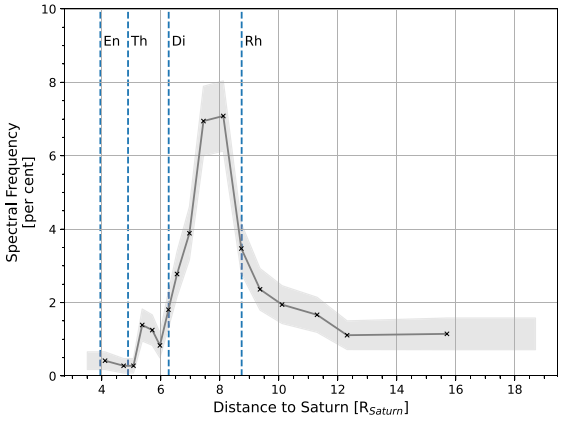

Figure 5. Profile of the relative frequency distribution of Type 5 along the radial extent of the E ring. The grey shaded area states the standard error of the mean: $SEM = 100 * \sqrt{p_{Type} * (1 - p_{Type})/n_{tot}}$, *with* $p_{Type} = n_{Type}/n_{tot}$, where n_{Type} here is the number of Type 5 detections in the respective bin and n_{tot} is the preassigned bin size of 720 spectra bin^{-1}. The dashed lines mark the mean orbital distances of the icy moons Enceladus (En), Tethys (Th), Dione (Di), and Rhea (Rh).

Unfortunately, higher salt concentrations cannot be measured with this analogue experiment due to the incipient precipitation of ice and salts at the instrument nozzle outlet that blocks the water beam. However, even this lower limit would be a salt concentration at least one order of magnitude higher than the salt concentrations inferred for Type 3 particles (≈ 0.2–0.3 mol L^{-1} of salts; Postberg et al. 2009a). We also see (Fig. 4), that the LILBID delay time and thus the particle impact speed on to CDA–CAT, clearly affects the resulting peak amplitude ratio, indicating that the impact speed also plays an important role in the formation of Type 5 spectra.

In order to identify the source of Type 5 particles, we conduct a radial mapping of the type's frequency relative to the other E ring ice particles (Fig. 5). From the overall 180 identified spectra of Type 5, 142 are considered for this mapping due to the limitation of the CDA–BS (see Section 2.1). Unexpectedly, the Type 5 particle proportion has a sharp maximum (≈7 per cent) at distances between 7 and 8.5 R_{Saturn}. They are least frequently detected (<0.5 per cent)

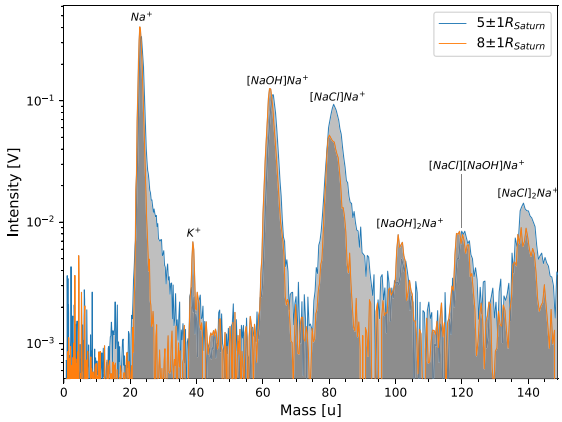

Figure 6. Sum-spectra of NaCl-rich Type 3 for the two distance regimes of 4–6 R_{Saturn} (23 spectra, blue line) and 7–9 R_{Saturn} (11 spectra, orange line) from Saturn.

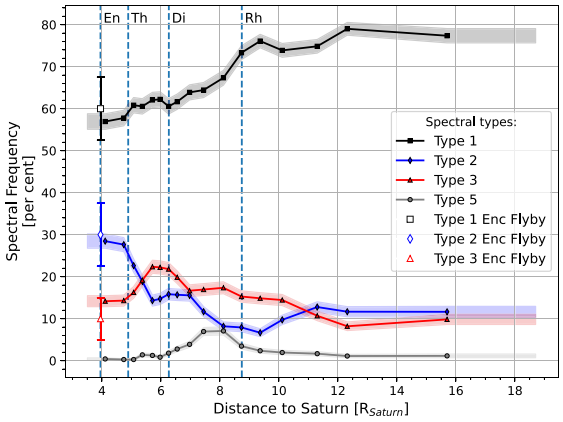

Figure 7. Profile of the relative spectral frequency distribution of all particle types along the radial extent of the E ring. The absolute particle number density of E ring particles decreases by several orders of magnitude for the shown radial range (Srama et al. 2011). The colour-shaded areas represent the respective standard error of the mean (see Fig. 5) The dashed lines mark the mean orbital distances of the ice moons Enceladus, Tethys, Dione, and Rhea. The blank symbols at 3.95 R_{Saturn} represent the spectral frequencies of Type 1–3 in the E ring close to the Enceladus plume (Postberg et al. 2011, 2018b).

at the orbital distance between 4 and 5 R_{Saturn}, just outside the orbit of Enceladus (3.95 R_{Saturn}), which marks the densest region of the E ring. As we will discuss later in detail (see Section 4.1), this argues against a direct Enceladus origin of this very salty, compositional type. Instead, they could represent old, heavily space weathered Type 3 particles, accumulating in the E ring near the orbit of Rhea.

3.2. Analysis of Type 3 spectra

To further investigate this hypothesis and take into account our NaCl-based laboratory results, we analyse the sum-spectra of NaCl-dominated∗ Type 3 CDA spectra (Fig. 6), obtained in two separate E ring regions at distances of 4–6 R_{Saturn} (inner) and 7–9 R_{Saturn} (outer) from Saturn. A distinct trend is apparent for the $Na^+/[NaCl]Na^+$ peak amplitude ratio, with the ratio in the inner region (3.4 ± 0.7) being only about half of the ratio that is found in the outer region (6.7 ± 2.0). From the experimental results (Fig. 4), showing $^{23}Na^+/[^{23}Na^{35}Cl]^{23}Na^+$ peak ratios increasing with overall salt concentrations, we therefore infer that the salt-concentrations in Type 3 particles increase with radial distance from Saturn. This supports the hypothesis that Type 5 particles evolve from Type 3 particles. Interestingly, the Na^+/K^+ peak amplitude ratios of 178.1 ± 37.1 (inner) and 73.9 ± 22.3 (outer) for these Type 3 spectra indicate a distinct, distance-dependent increase of the potassium signal, whereas the $Na^+/[NaOH]Na^+$ amplitude ratios of 3.0 ± 0.6 for the inner region and 3.0 ± 0.9 for the outer show no clear trend.

3.3. Spatial E ring analysis

The spectral frequency profile of the other spectral types of ice particles (Fig. 7) shows distinct changes from the densest regions of the E ring to the thinner, outer part. Just outside the orbit of Enceladus the original Types 1, 2, and 3 are in good agreement with the proportions found in the E ring close to the Enceladus plume (Postberg et al. 2011, 2018b; Fig 7 blank symbols). Type 1 is then continuously more frequently detected with increasing distance from Saturn from ≈55 per cent at 4 R_{Saturn} to almost 80 per cent in the outer E ring. The relative frequency of Type 2 declines with distance to Saturn from almost 30 per cent to a minimum (≈8 per cent) at around 8–9 R_{Saturn}. The Type 3 proportion first grows to a frequency maximum (≈22 per cent) at around 6 R_{Saturn}, near the orbital distance

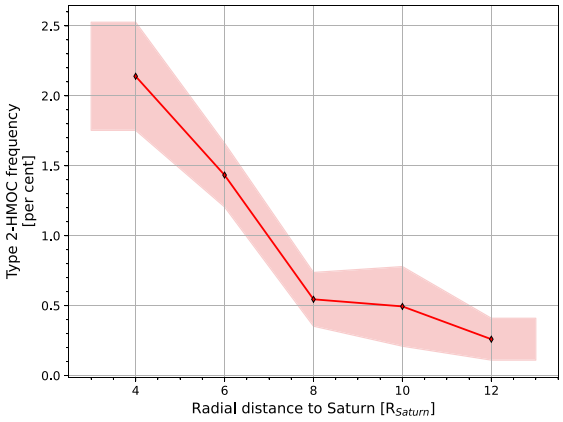

Figure 8. Profile of the relative spectral frequency of the Type 2–HMOC subtype along the radial extent of the E ring (based on data from Postberg et al. 2018a).

of Dione and then drops again continuously to about 9 per cent in the outer E ring. Outside 12 R_{Saturn} the spectral frequency trends of all particle types plateau.

Similarly, we analyse the radial distribution of the relative frequency of the Type 2–HMOC subtype, in which complex refractory organics are present ('High-Mass Organic Cations'; Postberg et al. 2018a), along the radial extent of the E ring (Fig. 8). Here we observe again a declining trend, as with the distribution of the general Type 2. From the orbital distance of Enceladus out to 12 R_{Saturn} the relative frequency of Type 2–HMOC drops by a factor of about 10.

4. DISCUSSION

4.1. Origin of Type 5 grains

Our work revealed a characteristic set of properties for Type 5 particles: Indications for a salt/water ice composition (Fig. 2 and Tables S2 and S3) with very high salt concentrations (>4 mol L^{-1}),

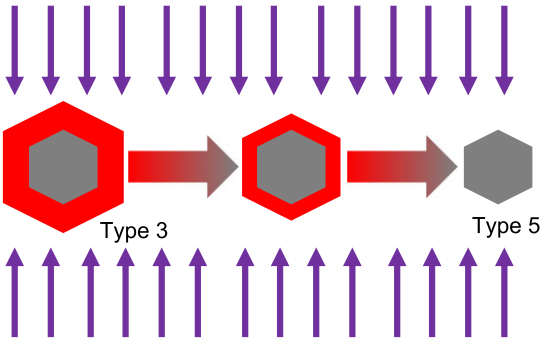

Figure 9. Simple idealized schematic on how the Type 5 particles possibly form from Type 3 particles via erosion by plasma sputtering (arrows). The ongoing bombardment by ions and electrons continuously erodes the salt-poor ice shell (red) while the salt-rich ice core (grey) is mostly unaffected. Since the absolute amount of salt remains about constant or is removed more slowly than the ice, salt concentrations increase throughout the process and eventually suppress other mass lines in the spectra, producing the reported spectral appearance of Type 5.

likely originating from inside the E ring with an increased probability of detection far outside the orbit of Enceladus (Fig. 5). Thus, we suggest here that Type 5 particles represent extremely salt-rich water ice particles, secondarily formed inside the E ring over time. The most likely predecessor particles are the salt-bearing Type 3 particles, ejected by Enceladus (Postberg et al. 2009a, 2011). Plasma sputtering would be the responsible transformation mechanism to erode E ring particles (Jurac et al. 2001a; Jurac, Johnson & Richardson 2001b; Johnson et al. 2008; Hsu et al. 2011a, b, 2015). During the formation of Type 3 particles, ice and salt are likely separated by the freezing process and it is possible that salts accumulate preferentially in the particle core. The continuous erosion of the salt-poor shell by plasma sputtering (Fig. 9), preferentially removing the water ice, would consequently lead to an increasing salt concentration over time. Even if the salt is not accumulated around the centre but elsewhere in the particle (e.g. in the form of salt veins) an increase of the salt concentration over time is still possible when considering different sputtering rates of water ice and salt. As discussed by Hsu et al. (2011b) for Saturnian stream particles, water ice exhibits several times higher sputtering rates than silicate (Tielens et al. 1994; Guillet, Jones & Pineau Des Forêts 2009). Based on this, salts, as another mineral component, can be assumed to be also more resistant against sputtering than water ice, which again would result in a preferential erosion of the water ice, causing an increase of the salt concentration over time.

Such a correlation of particle age and salt concentration is also supported by our observations in the NaCl-rich Type 3 spectra at different distances to Saturn (Fig. 6) in combination with our laboratory results of different salt concentrations (Fig. 4). The NaCl-rich Type 3 particles from larger distances to Saturn tend to be older than those found at lower distances, due to the outwards-directed particle migration, driven by plasma drag (Dikarev & Krivov 1998). Our results (Figs 4 and 6) suggest that salt concentration in Type 3 particles grows with distance to Saturn and thus age. The actual transition to Type 5 would then take place when the salt concentration has grown beyond a concentration threshold, that ultimately causes the suppression of salt cluster-related mass lines. The remaining elemental mass lines of $^{23}Na^+$ and $^{39}K^+$ then produce the characteristic spectral appearance of Type 5.

It is also important to point out, that the observed delay time differences in our laboratory results (Fig. 4) indicate that – in addition to high salinity – higher impact speeds suppress the formation of salt cluster ions (here $[^{23}Na^{35}Cl]^{23}Na^+$). This conclusion is based on the reverse correlation of LILBID instrumental delay time and CDA impact speed (Klenner et al. 2019) and could ultimately result in the enhancement of Type 5 spectral characteristics from ice particles that would produce Type 3 spectra at lower impact speeds. Hence, in future CDA spectra revisions we expect to see a relatively higher proportion of Type 5-like spectra in CDA data from high-speed Enceladus plume flybys (e.g. E5; Postberg et al. 2011) or during high-speed passages of the inner E ring (Linti et al., in preparation) compared to those of low speed plume flybys (e.g. E17; Postberg et al. 2018b).

However, if Type 5 really stems from Type 3 and only water ice is eroded in the process of transformation, both types should show comparable ratios of sodium and potassium salts and thus $^{23}Na^+/^{39}K^+$ peak amplitude ratios. But as reported earlier, the Type 5 archetypes (early triggered and a good spectrum quality) mostly exhibit moderate ratios (<3; Fig. 3), while the vast majority of Type 3 spectra is dominated by sodium salts and on average exhibits very high $^{23}Na^+/^{39}K^+$ peak amplitude ratios of about 100 and larger (Postberg et al. 2009a). We suggest here two scenarios that may explain this discrepancy.

First, we cannot rule out that besides the water ice also parts of the salts are eroded. For example if the assumed salt-rich ice core of Type 3 particles is not compositionally homogeneous but exhibits a further stratification into a sodium-rich subshell and potassium-rich core, parts of this subshell could also be eroded by the plasma sputtering. This would result in a loss of sodium salts relative to the potassium salts, causing the observed reduction of the $^{23}Na^+/^{39}K^+$ peak amplitude ratio. In this context, also the preferred erosion of sodium over potassium, as pointed out by Johnson et al. (2002) based on sputtering of Na and K on Europa's icy surface, could be a possible explanation.

The second explanation is an observational bias, in which spectra, with a relatively strong $^{39}K^+$ mass line, were preferentially identified as Type 5. Type 5 spectra, produced by grains with $^{23}Na^+/^{39}K^+$ peak amplitude ratios typical for Type 3, would consist of a single peak, the mass line $^{23}Na^+$, which in the case of line triggering would even be truncated. This reduced the chance that the spectra were identified as valid spectra by CDA's onboard software and transmitted to Earth. Moreover, even if transmitted, the calibration of single peak spectra is generally difficult without at least one second point of reference. For example the numerous line-triggered and thus single peak Type 5 spectra in this work, just showing the $^{39}K^+$ mass line, could only be identified as $^{23}Na^+$-triggered, based on the shift parameter exhibiting a t_0 value of around -2.25 µs (see Section 2.1), when the single peak is assigned to the mass 39 u. For spectra with $^{23}Na^+$ being the actual single peak, this approach would not work however. Hence, it is likely that CDA spectra of Na-dominated 'Type 5-Na' grains are much more abundant in reality than the K-rich Type 5 population of this work. They do not show up in the Type 5 data set because the rare cases dominate, that exhibit sufficient potassium to allow a mass calibration. We conclude that the Type 5 spectra rich in both Na and K salts reported here, are likely to be the 'tip of the iceberg' of a much more numerous, very high salinity E ring population, dominated by sodium salts.

4.2. Implications for E ring dynamics

A remarkable finding is that the peak in the relative frequency of Type 5 particles lies between the orbits of Dione and Rhea (Fig. 5). Since we have no indication of other sources for salt rich dust in this

E ring region, these grains probably still originate from Enceladus. As previously mentioned, we suggest that during the time spent in the circumplanetary environment the nearly pure ice mantles of the Type 3 grains are increasingly eroded by sputtering due to magnetospheric plasma (Fig. 9). Simultaneously, the drag exerted by the plasma will transport the grains radially outward, away from Enceladus (Dikarev & Krivov 1998), such that grains in more distant orbits from their source will tend to be older. Thus, with increasing distance from Enceladus, an increasing fraction of the Type 3 particle population is indeed expected to turn into Type 5 (Fig. 7).

The time per radial distance that a grain is exposed to plasma sputtering will be increased if the outward orbital migration of dust particles is slowed down by other dynamical processes. One such process has been described by Mitchell, Colwell & Horányi (2005). In the E ring, dust particles are subject to charging, by collisions with electrons and ions from magnetospheric plasma, including the effect of secondary electron emission, and photo emission due to Solar UV. As a result, grains acquire a negative charge within approximately 7–8 R_{Saturn} from Saturn and a positive charge radially outward from this distance (Horanyi, Burns & Hamilton 1992; Kempf et al. 2006). A minimum of the negative charge, and thus the equilibrium potential Φ, has been measured at an approximate orbital distance of 7 R_{Saturn} (Kempf et al. 2006). As outlined by Mitchell et al. (2005), owing to the finite charging times (the time that it takes a grain to acquire the equilibrium potential), a charged grain on an eccentric orbit can exchange energy with the magnetospheric, corotational electric field. In particular, in regions where $\frac{d\Phi}{dr} < 0$ (i.e. roughly inside 7 R_{Saturn}) the grain will gain energy leading to an increase of its semimajor axis. In regions where $\frac{d\Phi}{dr} > 0$ (outside 7 R_{Saturn}) the grain loses energy and the semimajor axis decreases. Thus, when acting on top of other dynamical processes induced by perturbations from solar radiation, plasma drag as well as the planetary magnetic field and higher-order gravity (Horanyi et al. 1992; Dikarev & Krivov 1998), this effect may lead to a slowdown of the outward orbital migration of E ring dust and with that to longer orbital residence times in the region between 7 R_{Saturn} and 8.5 R_{Saturn}. Since Type 5 presumably evolves via the process of plasma sputtering from Type 3 particles, longer residence times in this region of the E ring should result in relatively more Type 5 particles evolving locally than in other ring regions, which is in good agreement with our results (Fig. 5). Therefore, this mechanism should be the reason for the Type 5 frequency peak between 7 and 8.5 R_{Saturn}. The frequency decrease of Type 5 at distances larger than 8.5 R_{Saturn} from Saturn (Fig. 5) can also be explained by this mechanism. When finally migrating out of the 7–8.5 R_{Saturn} region, the Type 5 particles, already being smaller due to their sputtering-driven evolution from Type 3, have been eroded to even smaller sizes, if not completely. This increases the chance that they have declined below the detection threshold of CDA's CA for the encountered impact speeds of around 6–8 km s^{-1} (Table S2) and thus being invisible for CDA. Moreover, smaller particles become increasingly susceptible to orbital perturbations by the Lorentz-force, eventually pushing the particles out of the Saturn system, as described for Saturnian stream particles (Hsu et al. 2011b). In addition to that, particles exhibit relatively short orbital residence times (compared to the 7–8.5 R_{Saturn} region). Thus, the outer E ring region can be expected to produce only few new Type 5 particles, sufficient to sustain the particle population at the observed low-frequency level (Fig. 5) but not enough to compensate the losses by sputtering.

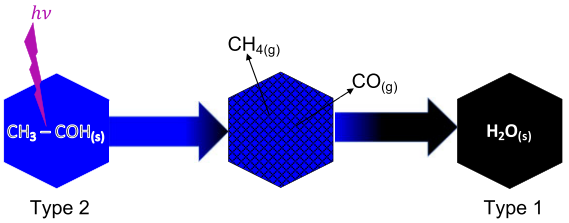

Figure 10. Simple idealized schematic on how Type 2 grains continuously loose part of their organic content by photochemical degradation until the total organic content drops below the spectral detection threshold and the respective spectra become Type 1. The shown molecule of acetaldehyde (ethanol) and the fragments are given as an example to illustrate the proposed loss by fragmentation into small, highly volatile molecular fragments, e.g. CH_x or CO. Also N-bearing organics can be present (Khawaja et al. 2019), which consequently produce fragments like CN or NH_y. (s) → solid, (g) → gaseous.

4.3. Weathering of Type 1, 2, and 3 grains

For the Type 5 grains we have suggested plasma sputtering acting in combination with the E ring particle dynamics as an explanation for the observed radial spectral frequencies profile. Another process capable of altering the grain composition is photochemical degradation. These weathering processes, plasma sputtering, and photochemical degradation, affect the three main particle Types (1–3) differently, so that their action may contribute to or even explain the observed radial changes of the spectral frequencies of E ring grains.

For Type 2 particles we expect photochemical degradation to play a more important role. The organic molecules in Type 2 particles, typically either embedded in the centre (HMOC case; see Postberg et al. 2018a) or adsorbed on to the surface or near surface (Khawaja et al. 2019), are susceptible to degradation/fragmentation by solar or cosmic radiation (e.g. Allamandola, Sandford & Valero 1988). Thus, the ongoing radiation exposure is expected to continuously fragment organic molecules into successively smaller and thus more volatile species. This fragmentation proceeds until the molecules are so small (e.g. CH_x, CO, CN, OH or NH_y; Fig. 10), that they can escape the particles as volatiles. If sufficient organic fragments are removed from the ice particle, the grains' overall organic content drops below the CDA detection threshold and the resulting spectra are identified as Type 1. Such a transformation of Type 2 particles into secondary Type 1 is in good agreement with the opposing frequency trends of Types 1 and 2 along the radial extent of the E ring, as well as the decline in the relative frequency of Type 2–HMOC particles (Fig. 8). While the Type 2 population decreases with time, due to both plasma sputtering erosion and transformation into secondary Type 1, Type 1 can compensate losses from sputter erosion by replacement with transformed Type 2 particles.

For Type 1 particles, which are almost pure water ice with barely detectable traces of salts and no traces of organics, we consider that erosion by plasma sputtering is as well the most relevant weathering process (Hsu et al. 2011b). Photochemical degradation will mostly produce OH, O or H and related ions, which would escape from the particles as volatiles, leaving particle compositions effectively unaltered. Both processes will thus effectively lead to a shrinking of the ice grains without a compositional change that is measurable by CDA.

As indicated in the previous section, we expect Type 3 to behave in a similar way to Type 1, with plasma sputtering being the most relevant process, especially when considering the proposed transformation into Type 5. Photochemical degradation may still occur, but as for Type 1, alterations of the water ice fraction of Type 3 are not expected to produce detectable signatures in the spectra. However, one salt-related modification could be indicated by the observed, apparent constancy of the $[NaOH]Na^+$ mass line (Fig. 6). Based on the behaviour of the $[NaCl]Na^+$ mass line, one would expect $[NaOH]Na^+$ to behave similarly and decline as well with growing distance. However, NaCl and H_2O molecules could theoretically be subject to photochemical reactions, for example:

$$NaCl + H_2O \overset{+h\nu}{\rightarrow} NaOH + HCl.$$

While producing additional NaOH, potential by-products are either volatile and escape the particles (e.g. H, O, or OH) or do not show up in the cation mass spectra of CDA due to the ions' tendency to preferably form anions (e.g. Cl or HCl). Hence, such a photochemistry-driven NaOH replenishment might explain the behaviour of the $[NaOH]Na^+$ mass line.

The observed frequency peak of Type 3 near the orbit of Dione is, according to our current understanding, most likely to be a statistical effect, as no sources of salt-rich dust particles are known in this region. The absolute number density of all particle types drops radially outward (Srama et al. 2011) but the relative abundance of Type 2 drops drastically, while Type 3 grows. The number density of Type 3 therefore decreases more slowly than that of Type 2. We propose this happens because the organic bearing Type 2 grains are more susceptible to chemical alteration than the salty Type 3 grains. Alternatively, freshly produced Type 2 grains could be generally larger than Type 3. Since plasma drag induces a slower orbital migration for larger grains, this implies that a sizeable fraction of Type 2 remains confined for a longer time to a narrower annular region around Enceladus' orbit. Thus, the relative frequency of Type 3 increases between 5 and 6 R_{Saturn}. Further outward, the conversion from Type 3 to Type 5 then decreases the Type 3 proportion again.

5. SUMMARY AND CONCLUSION

Here, we have presented the first comprehensive, compositional map of the E ring along its radial extent, based on CDA mass spectra. Our results show radial changes of the relative particle type frequencies, which we interpret as driven by space weathering effects like photochemical degradation and plasma sputtering. This finding is supported by the discovery of a new, extremely salt-rich, particle type (Type 5). This type is preferentially detected in the region between the orbits of the moons Dione and Rhea, presumably forming from Enceladus' salt-bearing ice particles (Type 3) via plasma sputtering of the salt-poor ice component. This aspect of the spectral abundance of Type 5 provides indirect evidence for a particular radial dependence of the electromagnetic equilibrium potential of the E ring grains, as it was inferred from direct *Cassini* measurements in this region. Further evidence for the chemical (and by inference, spatiotemporal) evolution of E ring grains was found for Type 2. There are indications for the ongoing transformation of Type 2 particles into Type 1 particles, due to photochemical degradation of enclosed organics into volatile molecular fragments capable of degassing from the icy particles.

ACKNOWLEDGEMENTS

LN, FP, JKH, and NK were supported by the European Research Council under the European Union's Horizon 2020 research and innovation programme (Consolidator grant number 724908-Habitat OASIS). JKH also acknowledges support from German Research Foundation (DFG) grant number HI 2157/1–1. FK acknowledges support from NASA Habitable Worlds Program grant number 80NSSC19K0311. RS has been supported by the German Aerospace Centre through grant number 50OH1501.

DATA AVAILABILITY

The CDA data underlying this article are summarized in Table S2 and are archived on PDS–Small Bodies Node at https://sbn.psi.edu/pds/resource/cocda.html. The table of analysed CDA events and the laboratory data from the LILBID analogue experiments are available in the Zenodo public repository at https://doi.org/10.5281/zenodo.10161282.

REFERENCES

Allamandola L., Sandford S., Valero G., 1988, Icarus, 76, 225
Altobelli N. et al., 2016, Science, 352, 312
Baum W., Kreidl T., Westphal J., Danielson G., Seidelmann P., Pascu D., Currie D., 1981, Icarus, 47, 84
Cable M. L. et al., 2021, Planet Sci. J., 2, 132
De Pater I., Martin S. C., Showalter M. R., 2004, Icarus, 172, 446
Dikarev V. V., Krivov A. V., 1998, Sol. Syst. Res., 32, 128
Dougherty M. K., Khurana K. K., Neubauer F. M., Russell C. T., Saur J., Leisnerand J. S., Burton M. E., 2006, Science, 311, 1406
Fischer C., Postberg F., Altobelli N., Nölle L., Albin T., 2018, EPSC, 12, 1279
Guillet V., Jones A. P., Pineau Des Forêts G., 2009, Astron. Astrophys., 497, 145
Hansen C. J., Esposito L., Stewart A. I. F., Colwell J., Hendrix A., Pryor W., Shemansky D., West R., 2006, Science, 311, 1422
Hillier J. K. et al., 2007a, Mon. Not. R. Astron. Soc., 377, 1588
Horanyi M., Burns J. A., Hamilton D. P., 1992, Icarus, 97, 248
Horányi M., Juhász A., Morfill G. E., 2008. Geophys. Res. Lett., 35, 5
Hsu H. W., Kempf S., Postberg F., Trieloff M., Burton M., Roy M., Moragas-Klostermeyer G., Srama R., 2011a, J. Geophys. Res, 116, 10.
Hsu H. W., Postberg F., Kempf S., Trieloff M., Burton M., Roy M., Moragas-Klostermeyer G., Srama R., 2011b, J. Geophys. Res, 116, 23
Hsu H. W. et al., 2015, Nature, 519, 207
Johnson R. E., Leblanc F., Yakshinkiy B. V., Madey T. E., 2002, Icarus, 156, 136
Johnson R. E., Famá M., Liu M., Baragiola R. A., Sittler E. C., Jr., Smith H. T., 2008, Planet. Space Sci., 56, 1238
Jurac S., Johnson R. E., Richardson J. D., 2001b, Icarus, 149, 384
Jurac S., Johnson R. E., Richardson J. D., Paranicas C., 2001a, Planet. Space Sci., 49, 319
Kempf S. et al., 2008, Icarus, 193, 420
Kempf S., Beckmann U., Srama R., Horanyi M., Auer S., Gru¨n E., 2006, Planet. Space Sci., 54, 999
Kempf S., Beckmann U., Schmidt J., 2010, Icarus, 206, 446
Kempf S., Hor´anyi M., Hsu H.-W., Hill T. W., Juh´asz A., Smith H. T., 2018, in Schenk P. M., Clark R. N., Howett C. J. A., Verbiscer A. J., Waite J. H., eds, Enceladus and the Icy Moons of Saturn. Univ. Arizona, Tucson, USA, p. 195
Khawaja N. et al., 2019, MNRAS, 489, 5231
Klenner F. et al., 2019, Rapid Commun. Mass Spectrom., 33, 1751
Mitchell C. J., Colwell J. E., Horányi M., 2005, J. Geophys. Res., 110, 7
Nicholson P. D. et al., 1996, Science, 272, 509
Pang K. D., Voge C. C., Rhoads J. W., Ajello J. M., 1984, J. Geophys. Res., 89, 9459

Porco C. C. et al., 2006, Science, 311, 1393
Postberg F., Kempf S., Srama R., Green S., Hillier J., McBride N., Gru¨n E., 2006, Icarus, 183, 122
Postberg F., Kempf S., Hillier J., Srama R., Green S., McBride N., Gru¨n E., 2008, Icarus, 193, 438
Postberg F., Kempf S., Schmidt J., Brilliantov N., Beinsen A., Abel B., Buck U., Srama R., 2009a, Nature, 459, 1098
Postberg F., Kempf S., Rost D., Stephan T., Srama R., Trieloff M., Mocker A., Goerlich M., 2009b, Planet. Space Sci., 57, 1359
Postberg F., Schmidt J., Hillier J., Kempf S., Srama R., 2011a, Nature, 474, 620
Postberg F. et al., 2018a, Nature, 558, 564
Postberg F., Clark R. N., Hansen C. J., Coates A. J., Dalle Ore C. M., Scipioni F., Hedman M. M., Waite J. H., 2018b, in Schenk P. M., Clark R. N., Howett C. J. A., Verbiscer A. J., Waite J. H., eds, Enceladus and the Icy Moons of Saturn. Univ. Arizona, Tucson, USA, p. 129
Schmidt J., Brilliantov N., Spahn F., Kempf S., 2008, Nature, 451, 685
Showalter M. R., Cuzzi J. N., Larson S. M., 1991, Icarus, 94, 451
Spahn F. et al., 2006a, Science, 311, 1416
Spahn F. et al., 2006b, Planet. Space Sci., 54, 1024
Srama R. et al., 2004, Space Sci. Rev., 114, 465
Srama R. et al., 2011, CEAS Space J., 2, 3
Tielens A. G. G. M., McKee C. F., Seab C. G., Hollenbach D. J., 1994, Astrophys. J., 431, 321
Waite J. H. et al., 2006, Science, 311, 1419

SUPPORTING INFORMATION

Supplementary data are available at *MNRAS* online.

Table S1: Classification criteria of the three main compositional particle types, previously discovered in CDA E ring spectral data, relevant to this work.
Table S2: List of selected periods from the CDA data record used for the analysis (1 $R_{Saturn} = 60\,268$ km).
Table S3: List of minor peaks observed in at least two of the 180 Type 5 spectra. 'X' in the peak labels stands for unknown spectral feature and the number refers to the mean peak mass [u].
Table S4: Sample from the extended CDA spectra table available in full length online (https://doi.org/10.5281/zenodo.10 161 282).
Figure S1a–e: Selection of example spectra for the three compositional main types of ice particles (Table S1), including the mentioned but not considered mineral dust (Type 4) and stream particles.
Figure S2: Example Type 5 spectrum illustrating the order of magnitude of the minor peaks, only rarely observed in Type 5 spectra.
Figure S3: Example spectrum of the measurement of 4 molar salt-water mixture with a molar NaCl/KCl ratio of 9 and a delay time of 5.1 μs.

Please note: Oxford University Press is not responsible for the content or functionality of any supporting materials supplied by the authors. Any queries (other than missing material) should be directed to the corresponding author for the article.

This paper has been typeset from a Microsoft Word file prepared by the author.